Planetary and Space Science 122 (2016) 13–25

Contents lists available at ScienceDirect

Planetary and Space Science

journal homepage: www.elsevier.com/locate/pss

Calibration of the MESSENGER X-Ray Spectrometer

Richard D. Starr [a,*], Charles E. Schlemm II [b], George C. Ho [b], Larry R. Nittler [c], Robert E. Gold [b], Sean C. Solomon [c,d]

[a] Physics Department, The Catholic University of America, Washington, DC 20064, USA
[b] Space Department, The Johns Hopkins University Applied Physics Laboratory, 11100 Johns Hopkins Road, Laurel, MD 20723, USA
[c] Department of Terrestrial Magnetism, Carnegie Institution of Washington, Washington, DC 20015, USA
[d] Lamont-Doherty Earth Observatory, Columbia University, Palisades, NY 10964, USA

ARTICLE INFO

Article history:
Received 13 August 2015
Accepted 4 January 2016
Available online 17 January 2016

Keywords:
Mercury
X-rays
MESSENGER

ABSTRACT

The X-Ray Spectrometer (XRS) that flew on the MESSENGER spacecraft measured X-rays from the surface of Mercury in the energy range ~1–10 keV. Detection of characteristic K_α-line emissions from Mg, Al, Si, S, Ca, Ti, and Fe yielded the surface abundances of these geologically important elements. Spatial resolution as fine as ~40 km (across track) was possible at periapsis for those elements for which counting statistics were not a limiting factor. Four years of orbital observations have made it possible to generate from XRS spectra detailed elemental composition maps that cover a majority of Mercury's surface. Converting measurements to compositions requires a thorough understanding of the XRS instrument capabilities. The ground and flight calibration measurements presented here are necessary for the reduction and analysis of the X-ray data from the MESSENGER mission.

1. Introduction

Mercury is the closest planet to the Sun, and because it is so close, it is difficult to study from Earth-based observatories. Its proximity to the Sun also makes it very challenging to send spacecraft to this tiny planet. Four decades ago Mariner 10 flew by Mercury, twice in 1974 and once in 1975, providing a wealth of new information about the planet (Dunne, 1974). Despite the many accomplishments of that mission, the limited observation time accumulated during the three flybys left much unknown about Mercury's geologic history and the processes that led to the planet's formation. Mariner 10 remained the only spacecraft to visit Mercury prior to observations by the MErcury Surface, Space ENvironment, GEochemistry, and Ranging (MESSENGER) spacecraft. MESSENGER is a NASA Discovery mission that was designed to fly by and orbit Mercury (Santo et al., 2001; Solomon et al., 2001). It was launched in August 2004. Following one Earth flyby (29 July 2005), two Venus flybys (23 October 2006 and 4 June 2007), and three Mercury flybys (14 January 2008, 6 October 2008, and 29 September 2009), the MESSENGER spacecraft entered into orbit about Mercury on 18 March 2011. At the beginning of the orbital mission MESSENGER's orbit was ~12 h long and highly eccentric, with periapsis at ~200–500 km altitude and apoapsis at ~15,000 km altitude. In April 2012, the apoapsis altitude was reduced to ~12,000 km and the orbital period was reduced to ~8 h. One of the instruments in the MESSENGER payload was the X-Ray Spectrometer (XRS), designed to determine the surface elemental composition of the planet by measuring solar-induced X-ray fluorescence (Schlemm et al., 2007).

XRS orbital operations began on 23 March 2011. X-ray fluorescence was routinely detected from the surface of the planet during both "quiet" Sun and flaring conditions whenever a sunlit portion of Mercury was within the XRS field of view. XRS can detect the characteristic X-rays of Mg, Al, and Si even during quiet-Sun conditions, but solar flares are required to produce measureable signals from elements at higher atomic number (Z) such as S, Ca, Ti, and Fe (Schlemm et al., 2007; Nittler et al., 2011). The XRS is sensitive to material within ~100 μm of the planetary surface.

Orbital X-ray fluorescence (XRF) experiments have flown on many planetary missions. X-ray spectrometers can provide surface composition measurements from any airless body. The first planetary XRF measurements were made by Luna 12 in 1968 (Adler et al., 1973) and then by the X-ray spectrometers on Apollo 15 and 16 (Adler et al., 1972a, 1972b). The Moon has been a frequent subject of XRF investigations, most recently by SMART-1 (Grande et al., 2007; Swinyard et al., 2009), SELENE (Okada et al., 2010), and Chandrayaan-1 (Narendranath et al., 2011; Weider et al., 2012a). X-ray spectrometers have also been flown to asteroids as part of the Near Earth Asteroid Rendezvous (NEAR) – Shoemaker

* Corresponding author. Tel.: +1 301 286 5073; fax: +1 301 614 6522.
E-mail address: richard.d.starr@nasa.gov (R.D. Starr).

http://dx.doi.org/10.1016/j.pss.2016.01.003
0032-0633/

mission (Trombka et al., 2000; Nittler et al., 2001; Foley et al., 2006; Lim and Nittler, 2009) and on Hayabusa (Okada et al., 2006).

MESSENGER is the latest planetary mission to include an XRF experiment as part of its science payload. Three gas proportional counters (GPCs) viewed the planet, and a Si-PIN detector mounted on the spacecraft sunshade viewed the Sun. The MESSENGER XRS incorporated an improved version of the NEAR – Shoemaker X-Ray Spectrometer design (Starr et al., 2000).

2. X-ray remote sensing

The primary source of X-ray fluorescent line emission from a planetary surface is the interaction of solar X rays with the surface (e.g., Yin et al., 1993). The most prominent fluorescent lines for the major elements Mg, Al, Si, S, Ca, Ti, and Fe are the K_α lines (1–10 keV). X-ray emission from the surface is strongly dependent on elemental composition, as well as the shape and intensity of the incident solar spectrum. The solar X-ray spectrum is not constant; it varies, on timescales of minutes to hours, in both intensity and slope. During quiet solar conditions, line emission from only a few light elements for which primary fluorescent lines are below 2 keV (Mg, Al, and Si) may be detected from orbit.

During periods of high solar activity the differential solar X-ray spectrum becomes much harder (i.e., stronger at higher energies) and more intense, enabling the measurement of heavier elements such as S, Ca, Ti, and Fe. Solar output is highly variable and may change by an order of magnitude or more within minutes. Greater solar activity yields better counting statistics within shorter integration times, and hence higher-resolution elemental abundance maps, especially for heavier elements such as Fe. Because of its variability, however, the Sun's output must be continuously monitored in order to obtain reliable results. An overview of X-ray remote sensing techniques for geochemical analysis has been given by Yin et al. (1993).

3. Instrument description

3.1. Planetary sensors

The MESSENGER XRS planet-pointing detector package included three large-area (10 cm^2) sealed gas proportional counters with thin (25 μm) Be windows. These three GPCs along with their measurement circuitry comprised the Mercury X-ray Unit (MXU). The MXU was situated within the MESSENGER payload adapter ring (Schlemm et al., 2007). Gas proportional counters were selected for the MESSENGER XRF experiment because of their flight heritage and large effective area. The large area provided the necessary sensitivity to achieve good counting statistics for short counting times (~minutes). The Be windows absorbed the lower-energy X-rays (below ~1 keV) that would otherwise dominate the detector count rate. Each counter was filled with P-10 gas (90% argon and 10% methane) to an absolute pressure of 1500 mbar. The bias voltage on each of the gas counters was ~1420 V during cruise and the first year of orbital operations. It was raised in the second year of orbital operations, as discussed below. The Be window was supported by a rectangular Be support structure. The

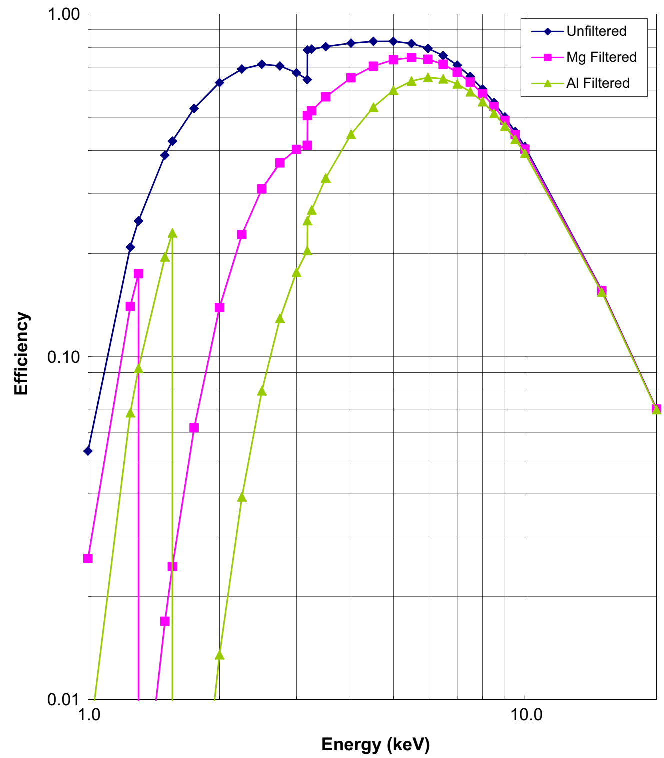

Fig. 1. Modeled detector efficiency versus energy for MESSENGER gas proportional counters (GPCs). Model results have been multiplied by 0.9 to take into account the non-uniform response of the GPCs, as discussed in the text. The effect of the Mg and Al filters at low energies is clearly seen. The break in the curve near 3.2 keV is the argon K-edge. The 25 μm-thick Be window attenuates the lower-energy X-rays in all three detectors.

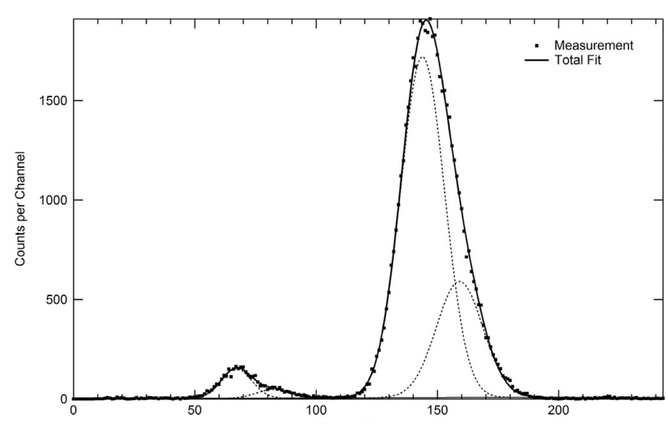

Fig. 2. Response of an unfiltered MESSENGER gas proportional counter to a radioactive ^{55}Fe source. The fit to the spectrum (solid line) is accomplished by including the K_α (5.90 keV) and K_β (6.49 keV) Mn lines in both the full-energy and escape peaks (dashed lines) plus a polynomial for the background. The fit for the full-energy K_α line gives a FWHM of 829 eV.

Table 1
Relative counting rate by cell number for the three GPCs.

Cell number				
1	2	3	4	5
6	7	8	9	10
11	12	13	14	15
GPC1 – Mg filtered				
84%	90%	90%	90%	88%
94%	100%	98%	99%	97%
80%	88%	87%	87%	84%
GPC2 – Al filtered				
84%	93%	93%	93%	92%
91%	97%	100%	97%	93%
75%	82%	83%	82%	79%
GPC3 – Unfiltered				
82%	93%	94%	93%	90%
89%	99%	99%	100%	100%
74%	83%	86%	84%	84%

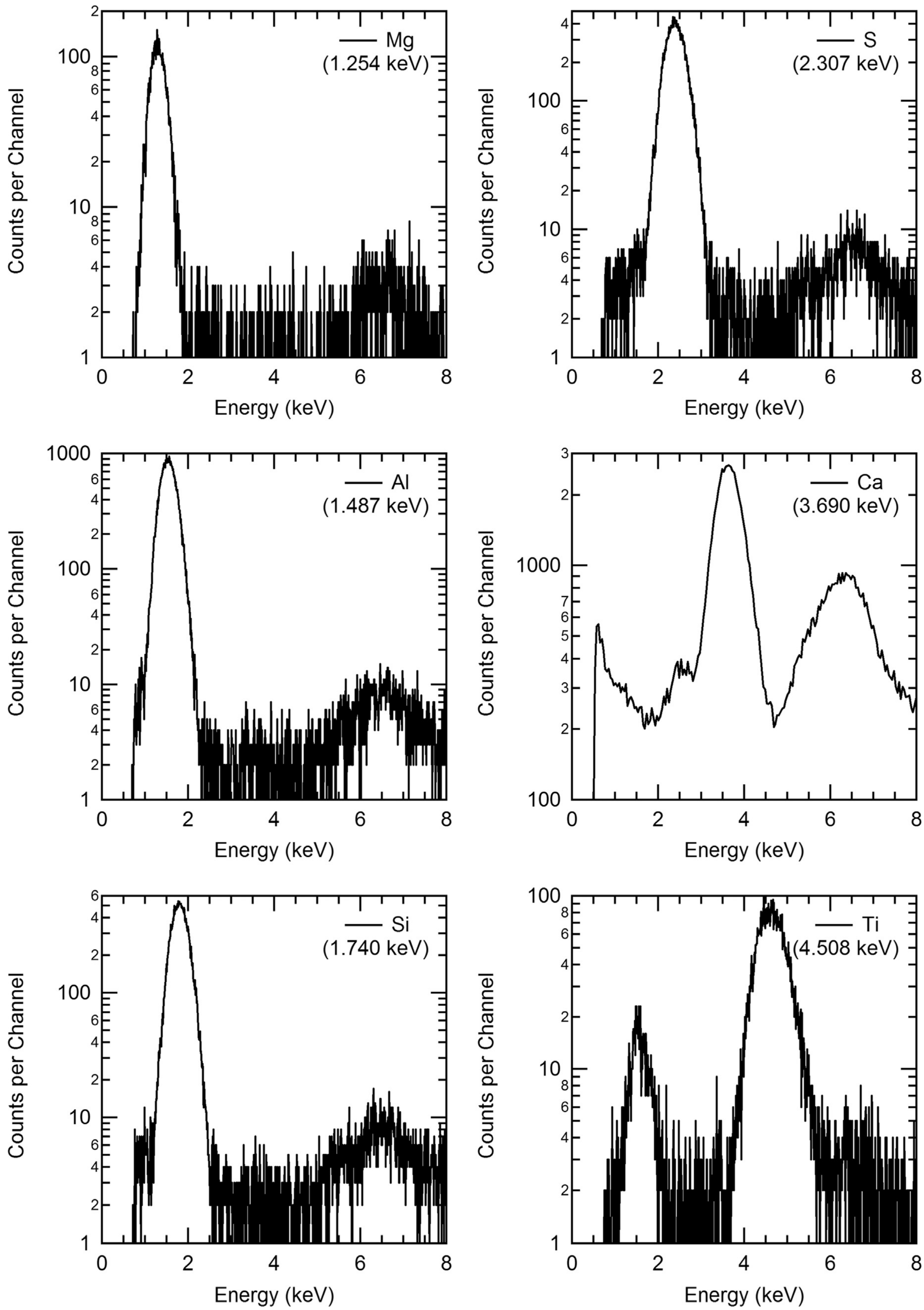

Fig. 3. Monoelemental pulse height spectra in an unfiltered MESSENGER gas proportional counter, generated with an alpha-particle source exciting targets of Mg, Al, Si, S, Ca, and Ti. The argon escape peak from the Ti target can be seen.

detector housing was titanium with a graphite liner to absorb Ti line emission from the housing. A Be–Cu honeycomb collimator provided a ~12° field of view (FOV), which was smaller than the planet at apoapsis and eliminated the X-ray sky background (Schlemm et al., 2007).

The GPC energy range was ~1–10 keV. This energy range includes the XRF K_{α} lines from several important rock-forming elements: Mg (1.254 keV), Al (1.487 keV), Si (1.740 keV), S (2.307 keV), Ca (3.690 keV), Ti (4.508 keV), and Fe (6.404 keV). The energy resolution of the gas proportional counters (~830 eV at 5.9 keV) was sufficient to resolve the X-ray lines above 2 keV, but not those below this energy. Accordingly, the MESSENGER GPC detectors, like those employed on the NEAR mission (Trombka et al., 2000), used balanced filters to resolve the closely spaced lines from Mg, Al, and Si. Two of the detectors had thin absorption filters, mounted externally. A Mg filter (4.5 μm) on one detector attenuated the Al and Si lines, and an Al filter (6.3 μm) on the other detector attenuated the Si line. The very steep absorption edges of the filters made the separation of the lower-energy lines possible. The third detector had no filter. The higher-energy lines from S, Ca, Ti, and Fe were resolvable by the GPCs.

Another similarity with the NEAR detectors was the use of rise-time discrimination to reduce the background induced by cosmic rays and gamma rays. The rise time of the signal pulses from a proportional counter due to particle and gamma-ray interactions is longer than that for X-rays. Rise-time discrimination can eliminate up to ~80% of these background events (Schlemm et al., 2007). A second background reduction technique used on MESSENGER, but not on NEAR, was that of anti-coincidence wires. These wires were located around the inner periphery of the gas tube (except by the entrance window) and parallel to the center anode wire. When a penetrating particle entered the proportional counter through the titanium wall, charge was collected by both the anti-coincidence and center anode wires, generating two signals. The event was eliminated by coincidence logic, which provided an additional ~80% reduction in background (Schlemm et al., 2007).

3.2. Solar monitor

The MESSENGER solar monitor was a small Si-PIN detector. Like the GPCs, its energy range was ~1–10 keV. The Solar Assembly for X-rays (SAX), which included the Si-PIN, a thermoelectric cooler (TEC), and a preamplifier, was mounted on the spacecraft sunshade (Leary et al., 2007). Because of the proximity to the Sun while in Mercury orbit, the detector aperture could be quite small, ~0.03 mm^2, and still provide good counting statistics within short collection times. To protect the solar monitor from the intense solar thermal input, three 25.4 mm Be foils covered the detector aperture. The solar monitor Si-PIN was biased at 110 V.

Solid-state detectors, like the MESSENGER Si-PIN, work best when cooled to temperatures well below 0 °C. At higher temperatures, leakage current increases, worsening energy resolution. At sufficiently high temperatures, the leakage current becomes so great that the bias on the instrument's field-effect transistor (FET) causes the preamplifier to saturate and effectively turn off the detector (Starr et al., 1999). Solid-state detectors may also suffer radiation damage in space that worsens energy resolution and reduces the useful operating temperature range. For these reasons, the Si-PIN detector for XRS was mounted on a miniature two-stage thermoelectric cooler that could cool the detector during normal operations and operate in a heater mode to provide in-flight annealing to counteract the effects of radiation damage (Schlemm et al., 2007).

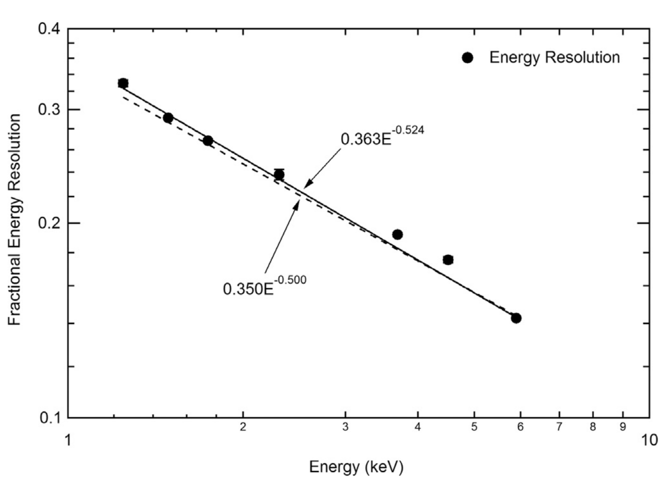

Fig. 4. The measured energy resolution of a gas proportional counter (data points) as a function of energy. The fit to the data (solid line) is a power law in energy that agrees well with the expected relationship; both the slope and proportionality constant were allowed to vary. The dashed line is a fit for which the slope is held to the theoretical value of −0.5.

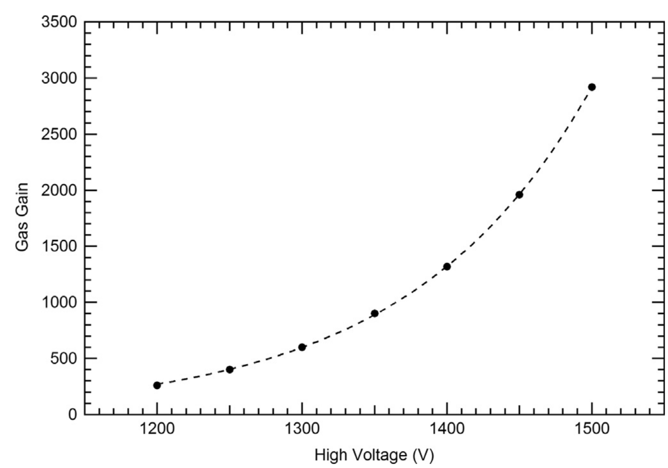

Fig. 5. Gas gain of the unfiltered GPC versus high voltage. The measured data (circles) are well fit by an exponential function (dashed line): gas gain=0.020038 $e^{0.0079261\ HV}$, where *HV* denotes high voltage.

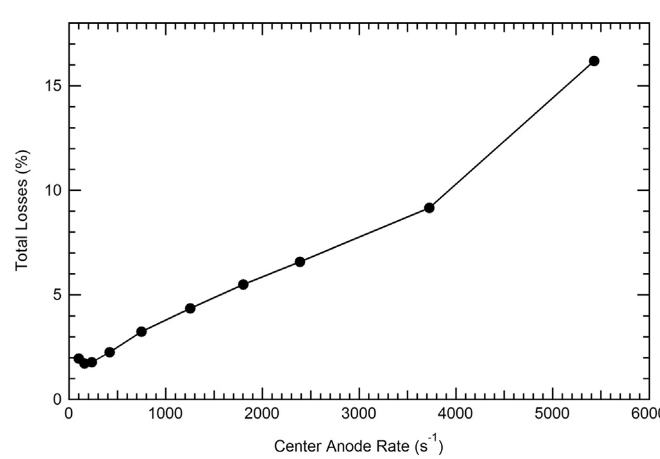

Fig. 6. Total event loss rate for the Al-filtered GPC due to both hardware and software effects.

4. GPC calibration measurements

4.1. Uniformity of response over window area

Uniformity of response over the 10 cm^2 active area of a GPC is important. Non-uniform electrical fields within the detector can cause detector efficiency to drop off near the edges of the window. Too great a drop off will result in an overall loss of efficiency. The rectangular Be support structure for the Be window of a GPC divided the 10 cm^2 active area into 15 smaller rectangles or cells. Detector response was mapped by moving a collimated ^{55}Fe radioactive source (5.9 keV) in front of each individual cell. The results are given in Table 1.

It is apparent from Table 1 that there was a reduction in relative efficiency with distance from the center cells. Combining the effect over all 15 cells gives a relative efficiency of ~90% for each GPC. There are two likely causes for this drop-off in efficiency. The first is that closer to the edges (cells 1–5 and 11–15) the interaction path length was shorter. This geometrical effect increased the likelihood of escape events, a process described in more detail in the next section. The second possibility is a non-uniform electric field in the counters. Such non-uniformity is to be expected at some level. The drop in efficiency is greater in the side cells (1–5 and 11–15) than in cells 6 and 10. This difference suggests that most of the fall-off in efficiency at the edges is due to poorer charge collection efficiency farther from the center anode wire.

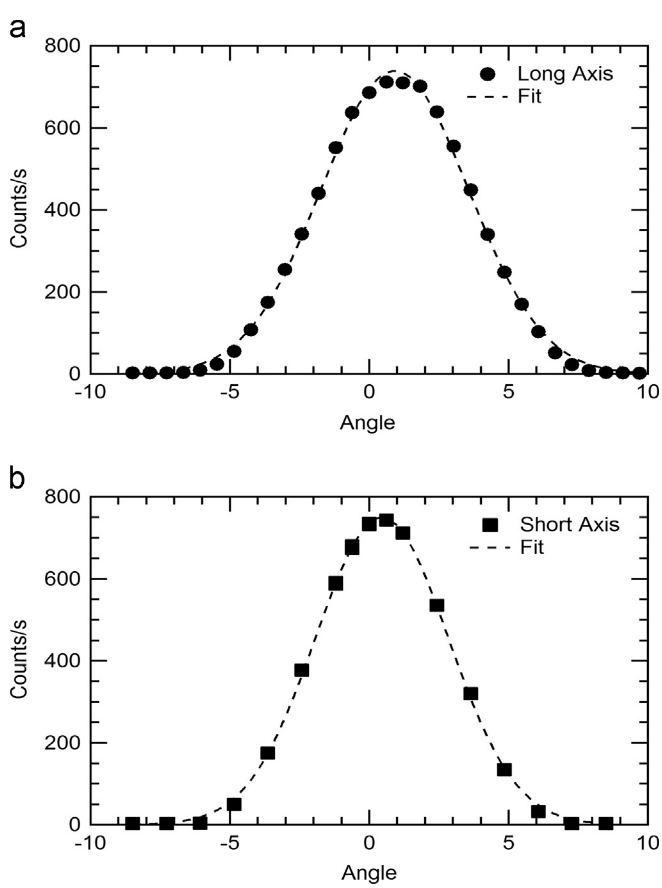

Fig. 7. The measured FOV of the XRS GPC (a) along the long axis (parallel to the center anode) and (b) along the short axis (perpendicular to the anode wire). The data points show the measurements, and the dashed black lines depict fits of Gaussian distributions to the data. FWHM = 6.38 ± 0.06° and FWTM = 11.68 ± 0.12° along the long axis; FWHM = 5.70 ± 0.05° and FWTM = 10.43 ± 0.09° along the short axis.

4.2. Efficiency

The MESSENGER GPCs were modeled with the Monte Carlo N-Particle eXtended (MCNPX) code (Pelowitz, 2005). The modeled efficiency versus energy for the three gas proportional counters is plotted in Fig. 1. A multiplicative factor of 0.9 has been applied to the modeled efficiencies to correct for the non-uniform field effects described above. The sharp features in the response of the Mg- and Al-filtered detectors at 1.30 and 1.56 keV, respectively, are the filter K-edges. The very sharp feature seen in all three detectors at 3.20 keV is the K-edge of Ar, the primary constituent of the proportional counter fill gas. This feature complicates the response of the proportional counters for energies above the absorption edge, because the resulting K_α X-ray, which is 2.97 keV for argon, may escape the detector. A corresponding escape peak will then appear in the spectrum at a differential energy below the full-energy peak equal to this characteristic energy. This effect can be seen in Fig. 2, which is the response of an unfiltered gas proportional counter to an ^{55}Fe source, which emits the Mn K_α and K_β lines at 5.90 and 6.49 keV, respectively. The fit to the measured pulse height spectrum (solid line) requires four peaks (dashed lines): one for the K_α line, one for the K_β line, and one for each of the two escape lines. The full energy peak for the K_α line is seen in channel 143.8. The

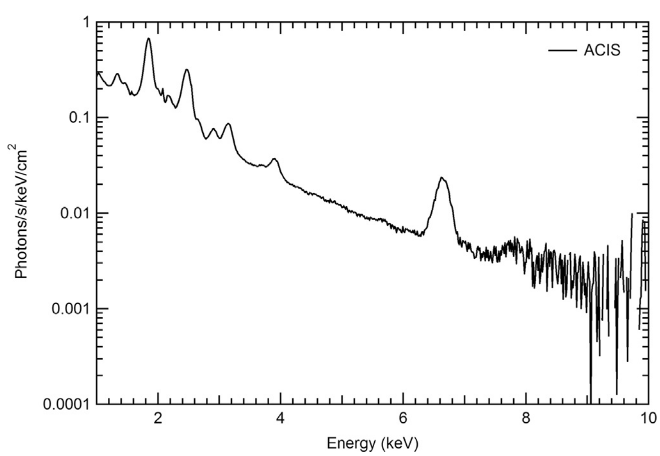

Fig. 8. Cas-A spectrum from the Chandra ACIS instrument (Weisskopf et al., 2002; Schwartz, 2004). This spectrum was generated by dividing the measured count rate spectrum by the instrument effective area.

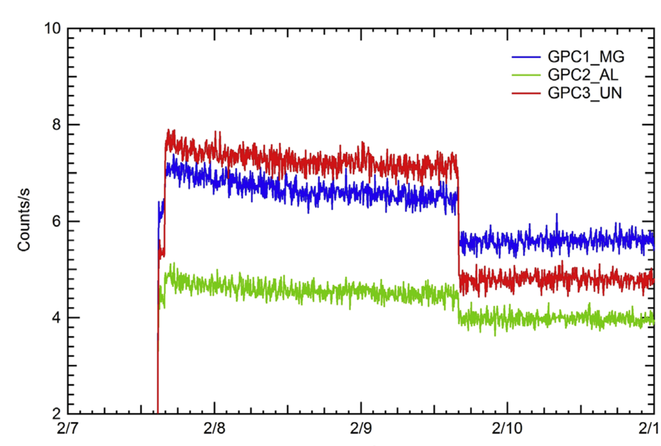

Fig. 9. GPC count rates during the February 2005 Cas-A observation, which began at ~16:00 UTC on 7 February and ended at ~16:00 UTC on 9 February. The background-subtracted count rates from Cas-A for the Mg-filtered (blue), Al-filtered (green), and unfiltered (red) detectors are 1.1 s^{-1}, 0.6 s^{-1}, and 2.5 s^{-1}, respectively.

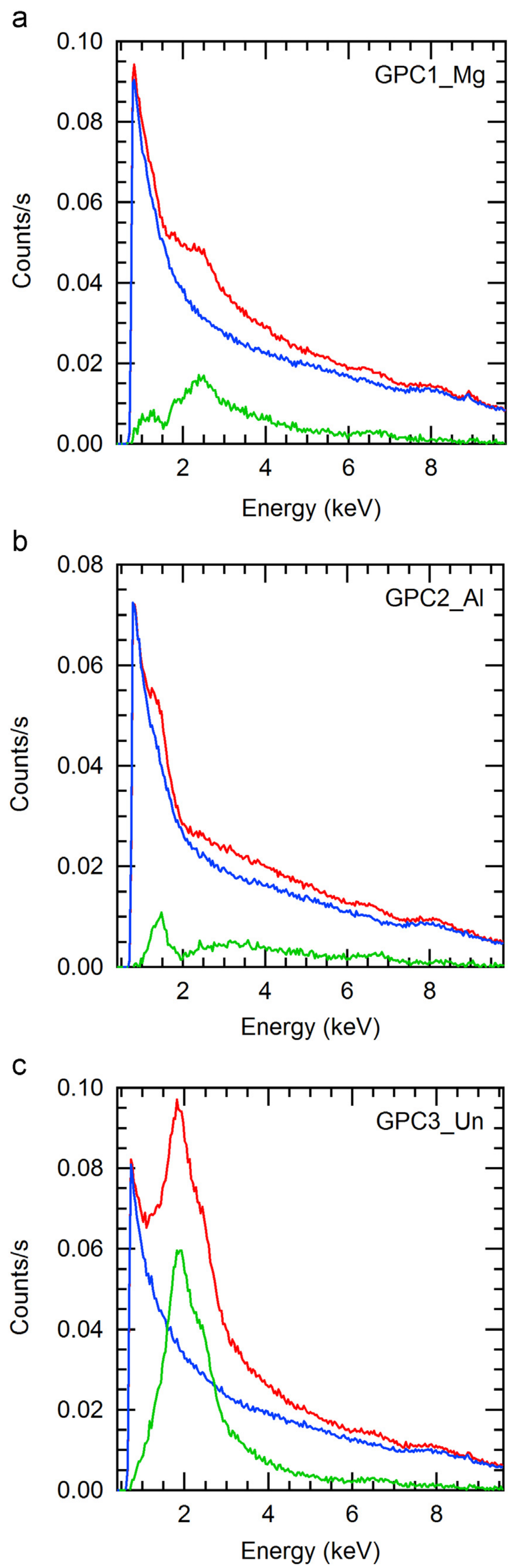

Fig. 10. Foreground (red), background (blue), and difference (green) measurements for (a) the Mg-filtered, (b) the Al-filtered, and (c) the unfiltered detectors made during the February 2005 Cas-A observation.

full energy peak for the K_α line is seen in channel 143.8. The corresponding escape peak is in channel 67.1.

The measured absolute efficiency of a MESSENGER gas proportional counter at 5.9 keV is 0.83 ± 0.005. This result was obtained by placing an ^{55}Fe source of known strength on axis and at a fixed distance from the detector. The error reflects statistical uncertainty only. Systematic errors are probably less than ~1%. Monte Carlo modeling of the MESSENGER gas proportional counters yields an absolute efficiency of 89% at 5.9 keV. When the effect of non-uniform charge collection is included, the modeled efficiency for an unfiltered GPC shown in Fig. 1 is 80% at 5.9 keV, in good agreement with the measurement.

4.3. Energy resolution

The energy resolution of gas proportional counters varies inversely as the square root of the energy,

$$\Gamma = 2.35\left(\frac{W(F+b)}{E}\right)^{1/2} \tag{1}$$

where Γ is the full-width at half-maximum (FWHM) as a fraction of the X-ray energy, W is the energy required to create an ion pair, F is the Fano factor, b is a parameter that characterizes the avalanche statistics, and E is the energy in keV (see, for example, Knoll, 1989). This equation represents the statistical limit for a gas proportional counter, i.e., the best response one can expect. For P-10 these parameters are, $W=0.026$ keV/ion pair, $F=0.17$, and $b=0.50$. The above equation then becomes:

$$\Gamma = 0.310E^{-1/2} \tag{2}$$

At 5.9 keV Eq. (2) implies an energy resolution of 12.8% or 0.753 keV. The energy resolution at 5.9 keV for the detector as shown in Fig. 2 is 0.829 keV, or about 14.0%, which is typical for all the XRS proportional counters. An increase of about 10% over the statistical limit is expected for these detectors due to electronic noise and non-uniformity of the anode wire.

The response of a proportional counter to six different X-ray lines is shown in Fig. 3. The pulse height spectra were generated by using an alpha particle excitation source on targets of Mg (1.254 keV), Al (1.487 keV), Si (1.740 keV), S (2.307 keV), Ca (3.690 keV), and Ti (4.508 keV). The fractional energy resolution of each of these six X-ray lines, plus the 5.9-keV line from ^{55}Fe, is plotted versus energy in Fig. 4. The solid line is a power law fit to the data with a slope of -0.524 ± 0.003 and a constant of proportionality of 0.363 ± 0.002. The dashed line is a fit for which the slope is forced to the theoretical value of -0.5. For this fit the proportionality constant is 0.350 ± 0.001.

4.4. Gas gain

Ionization electrons produced in proportional counters by the incident radiation generate an electron avalanche near the anode wire. This large increase in the number of primary electrons is called the gas multiplication factor or gas gain and depends primarily on gas pressure and the applied voltage (Knoll, 1989). Prior to launch, the high voltage of each of the GPCs was set so that the full energy range was ~1–10 keV. For the three detectors this voltage corresponded to 1425 V, 1414 V, and 1424 V for the Mg-filtered, Al-filtered, and unfiltered GPC, respectively. The GPC bias remained at these values until April 2012, when the high voltage was increased by 12 V for each detector to compensate for a ~10% loss in gain. The change in gain was gradual and had been observed to be slowly decreasing throughout the mission cruise

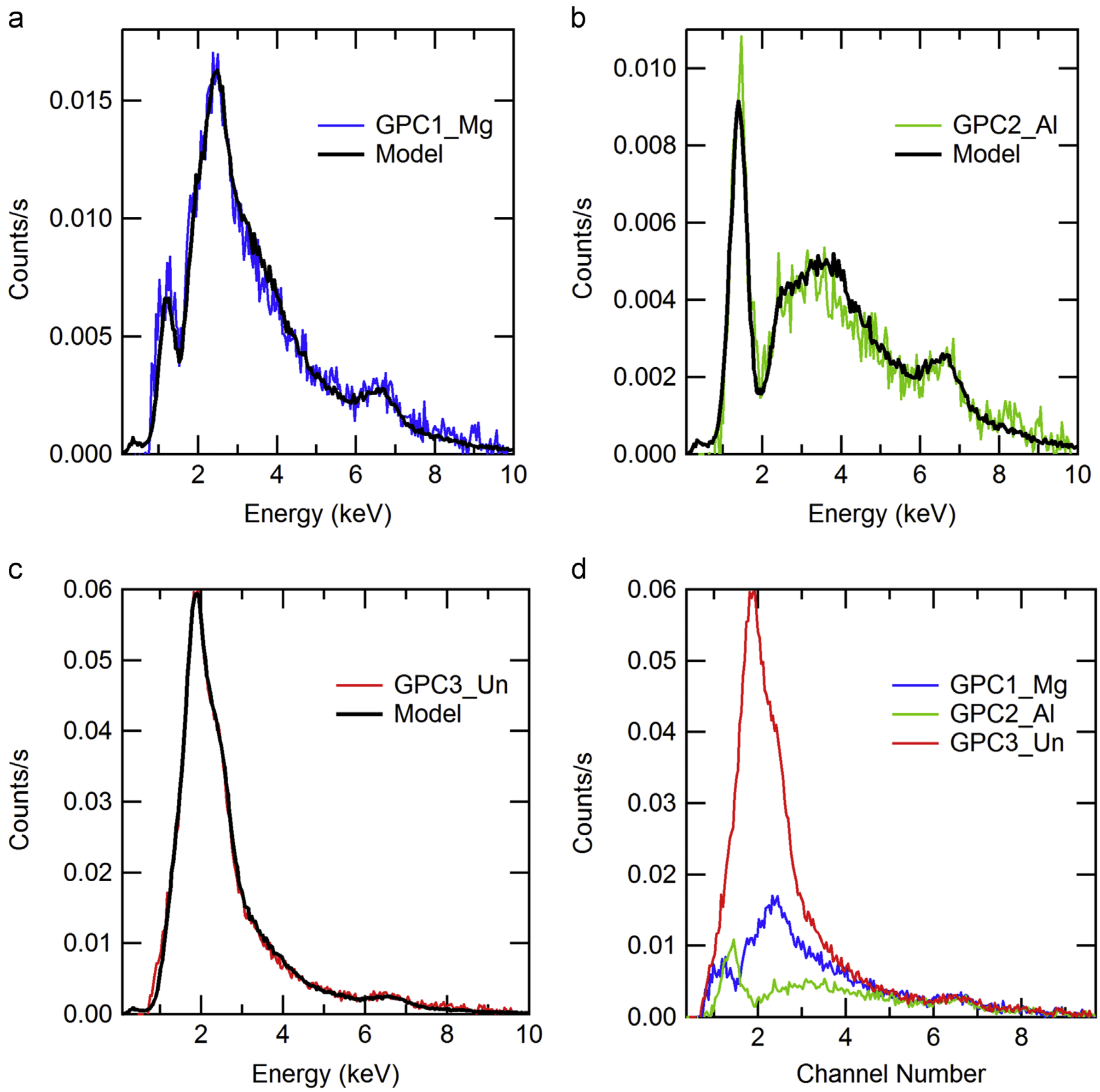

Fig. 11. Comparison of MCNPX model (black) with background-subtracted Cas-A measurement for (a) the Mg-filtered GPC, (b) the Al-filtered GPC, and (c) the unfiltered GPC. For comparison, background-subtracted measurements for all three GPCs are shown in (d). The best-fit filter thicknesses were 6.3 μm and 4.5 μm for the Al and Mg filters, respectively.

Table 2
Inferred filter thickness from Mg (1.25 keV) and Ca (3.69 keV) K_α-line transmission though the Mg and Al filters.

	Mg line (1.254 keV)	Ca line (3.690 keV)	
Filter	Measurement 1 (μm)	Measurement 1 (μm)	Measurement 2 (μm)
Mg	6.90 ± 0.18	5.28 ± 0.68	4.45 ± 0.10
Al	6.81 ± 0.13	6.61 ± 0.45	6.29 ± 0.05

phase, as illustrated by measurements of the X-ray flux from Cassiopeia A (Cas-A), a supernova remnant in the constellation Cassiopeia located at right ascension 350.9° and declination 58.8° (see below). It was only when the change became sufficiently great to affect spectral fitting that the decision was made to increase high voltage to correct for the gain loss. Fig. 5 shows the gas gain of the unfiltered GPC versus high voltage. The measured gain is well fit by an exponential function.

4.5. Live time

X-ray spectra collected during solar flare emissions provide the best data on the surface composition of Mercury. However, higher count rates may result in both hardware and software event losses. The event loss rate versus count rate for the Al-filtered GPC, obtained during pre-flight ground testing, is shown in Fig. 6. At rates up to 1000 s^{-1}, losses are no more than ~4%. Even at rates greater than 5000 s^{-1} the total losses are only about 16%. All the GPCs were tested and displayed results very similar to those shown in Fig. 6. Even for the largest flares observed by the MESSENGER XRS, GPC event rates rarely exceeded 1000 s^{-1}.

4.6. Field of view

A collimated ^{55}Fe source was used to measure the angular response of an XRS GPC over the entire FOV of the instrument with the Be–Cu collimator in place. The results are shown in Fig. 7a (long axis – parallel to the center anode wire) and Fig. 7b (short axis – perpendicular to the center anode wire). The FWHMs of the detector response are $6.38 \pm 0.06°$ and $5.70 \pm 0.05°$ for the long and short axes, respectively. The corresponding full widths at tenth maximum (FWTM) are $11.68 \pm 0.12°$ and $10.43 \pm 0.09°$. At a nominal periapsis altitude of 200 km, these FWTM values correspond to a spatial resolution (cross-track) of ~42 km.

4.7. Cassiopeia A observations

Beginning in 2005, the XRS was pointed toward Cas-A at least once each year during cruise to measure the GPC response. There were a total of 11 such observations; most observations collected ~48 h of on-target measurements, plus an equal amount of time off-target for background subtraction. The first Cas-A observation was in February 2005. One Cas-A observation was accomplished following Mercury orbit insertion, but with only ~12 h of on-target measurements.

A Cas-A spectrum collected by the AXAF (Advanced X-ray Astrophysics Facility) CCD (charged-coupled device) Imaging Spectrometer (ACIS) on the Chandra X-Ray Observatory (Weisskopf et al., 2002; Schwartz, 2004) is shown in Fig. 8. The MESSENGER XRS GPC background-subtracted count rates from Cas-A for the unfiltered, Al-filtered, and Mg-filtered detectors were ~2.5 s^{-1}, 0.6 s^{-1}, and 1.1 s^{-1}, respectively. The February 2005 count rate data are displayed in Fig. 9. The difference in count rates for the three GPCs is simply the result of the impact of the filters on GPC efficiency, as shown in Fig. 1. Counts in the two filtered GPCs are naturally lower than those in the unfiltered GPC. Because the Al filter is thicker than the Mg filter, its count rate is lowest.

The primary goal of the Cas-A measurements, made repeatedly throughout the MESSENGER mission, was to allow the XRS team to monitor the health and stability of the GPCs, but other valuable calibration information was obtained from these measurements as well, including GPC filter thickness and background rejection efficiency, both of which are discussed further below.

4.7.1. Filter thickness

The response of the three GPCs to the Cas-A observation of February 2005 is shown in Fig. 10. Foreground (red) and background (blue) measurements are shown as well as the difference spectrum (green). The response of the Mg-filtered and Al-filtered GPCs depends critically on the thickness of the filters. A detailed model of the GPCs (titanium housing, graphite liner, P-10 fill gas, Be grid, Be window, Mg and Al filters, and Be collimator) was created with MCNPX. The Cas-A spectrum (Fig. 8) was folded through the response of the three GPC MCNPX models and the filter thickness varied in order to find the best match to the measurements. The results of this process, which indicated that an Al filter thickness of 6.3 μm and a Mg filter thickness of 4.5 μm provided the best agreement with the measurements, are shown in Fig. 11. Manufacturer specifcations for the foils were 0.005 mm ± 10% for the Mg filter material and 0.006 mm ± 10% for

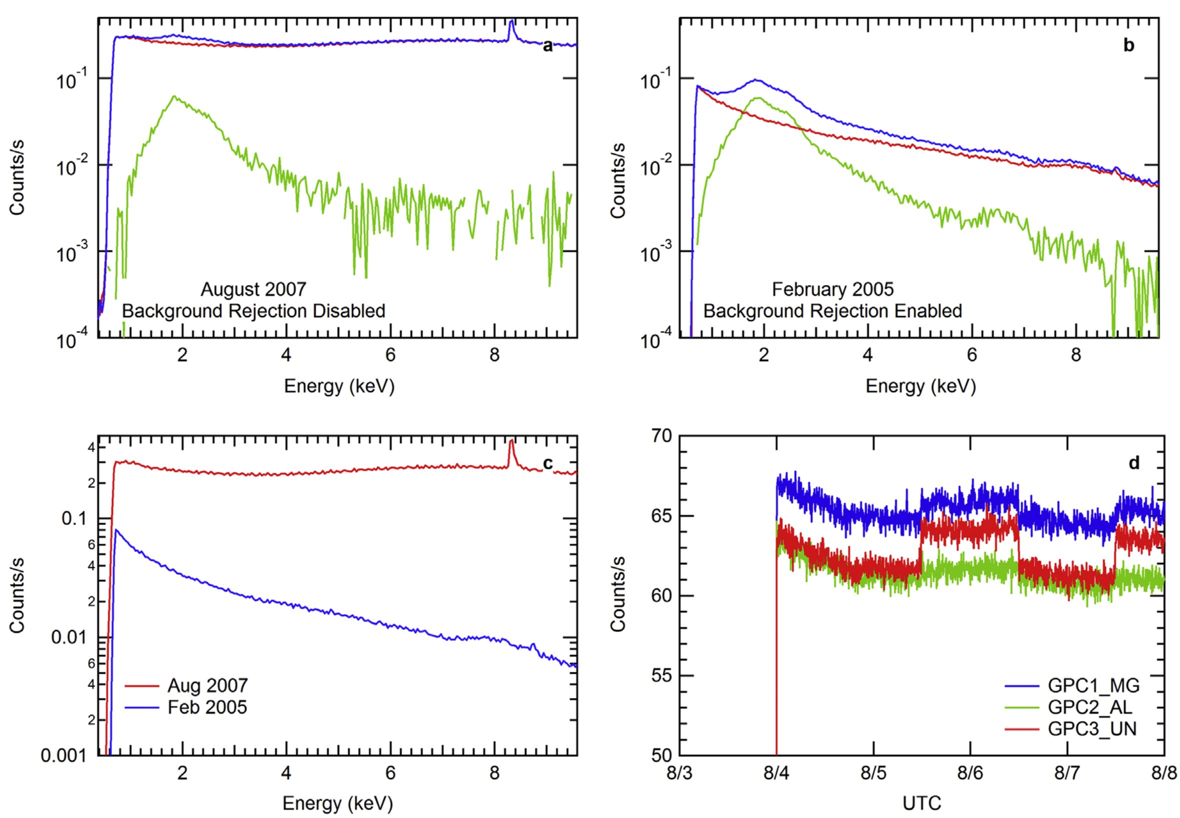

Fig. 12. Comparison of the unfiltered GPC Cas-A measurements (a) in August 2007 with background rejection disabled and (b) in February 2005 with background rejection enabled. Spectra on target are shown in blue, spectra off target in red, and difference spectra in green. (c) Comparison of background (off-target) spectra for the two observations. (d) Count rates for all three GPCs for the August 2007 period; these curves should be compared with those for February 2005 shown in Fig. 9. The August 2007 observation was limited to ~38 h of on-target measurements and was accomplished over two separate time periods, from ~11:50 UTC on 5 August to ~11:50 UTC on 6 August, and from ~11:50 UTC on 7 August to ~1:50 UTC on 8 August.

the Al filter material. The Cas-A results are in good agreement with these specifications.

Filter thickness was also measured prior to launch by irradiating Mg and Ca target material with an ^{55}Fe source. The resulting lines at 1.25 and 3.69 keV, respectively, were detected by a GPC, with no filter, then a Mg filter, and finally an Al filter. Other than the addition of the filters, the geometry was unchanged during the measurements. The reduction in peak count rate with the filters was used to calculate filter thickness. The results of these measurements are given in Table 2. The filter thicknesses inferred from the Ca-line measurements are in good agreement with the Cas-A values and the manufacturer specifications, 0.005 mm $\pm$ 10% for the Mg filter material and 0.006 mm $\pm$ 10% for the Al filter material. The Mg-line measurements, in contrast, give significantly higher filter values than those inferred from the Ca-line and the Cas-A measurements and are many standard deviations higher than the manufacturer specifications. For these reasons, the Mg-line measurements are considered outliers. The cause of the disagreement between the thicknesses inferred from Mg-line measurements and those derived from the Ca-line was never identified. Background was higher at low energies, and this situation may have contributed to peak-fitting errors, but no fully satisfactory explanation was ever identified. The best-fit Cas-A filter values are considered the most reliable measurement of the filter thicknesses and were used for all XRS data analysis.

4.8. Background reduction

As described above, the XRS gas proportional counters used rise-time discrimination and anti-coincidence circuitry to reduce background. In August 2007, an observation of Cas-A was made with rise-time discrimination and anti-coincidence logic disabled. Results for the unfiltered GPC are compared with the February 2005 observation in Fig. 12. This comparison demonstrates that rates were reduced by about an order of magnitude with background reduction enabled.

An important aspect of any background reduction technique is that it does not remove any substantial number of valid events. A comparison of the background-subtracted spectra for the February 2005 and August 2007 Cas-A observations is shown in Fig. 13 for

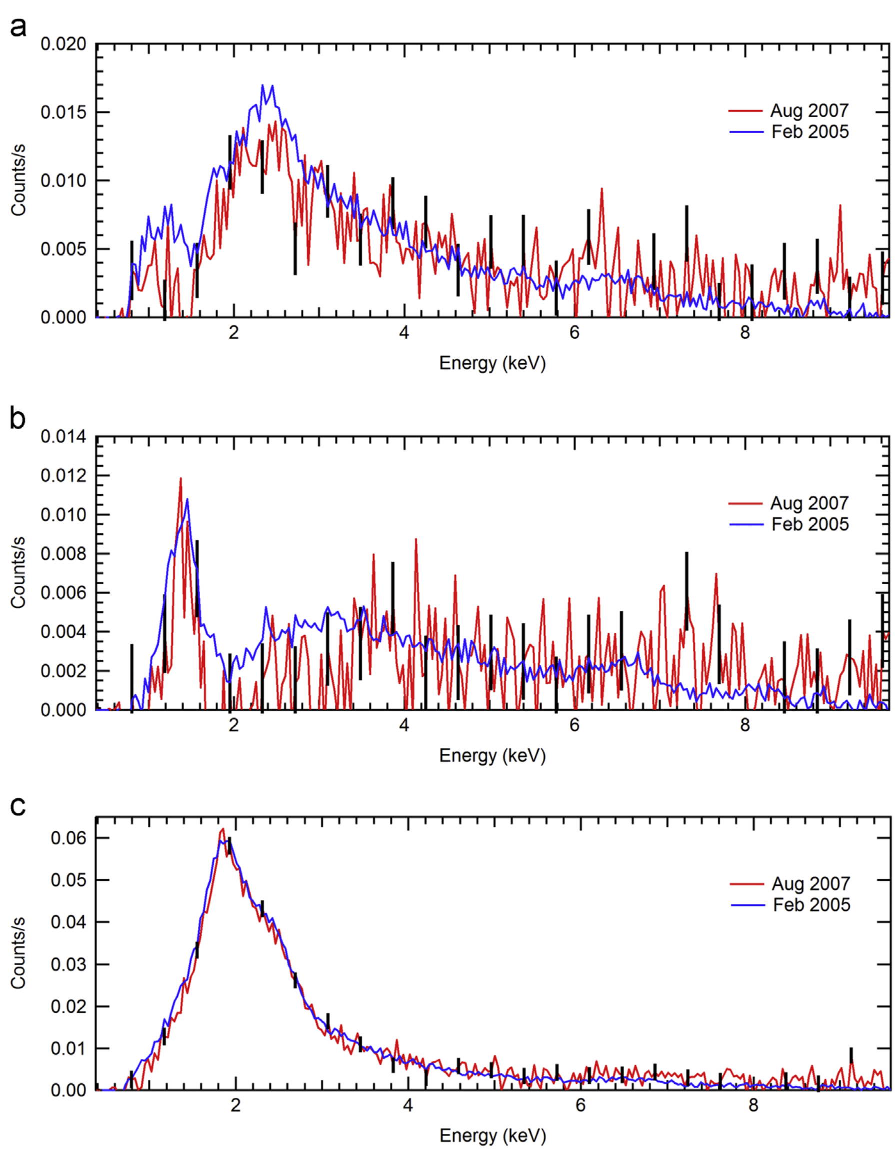

Fig. 13. Comparison of (a) Mg-filtered, (b) Al-filtered, and (c) unfiltered GPC measurements for Cas-A observations on August 2007 (red) and February 2005 (blue). Vertical black bars show the statistical uncertainty (one standard deviation) for the August 2007 measurement.

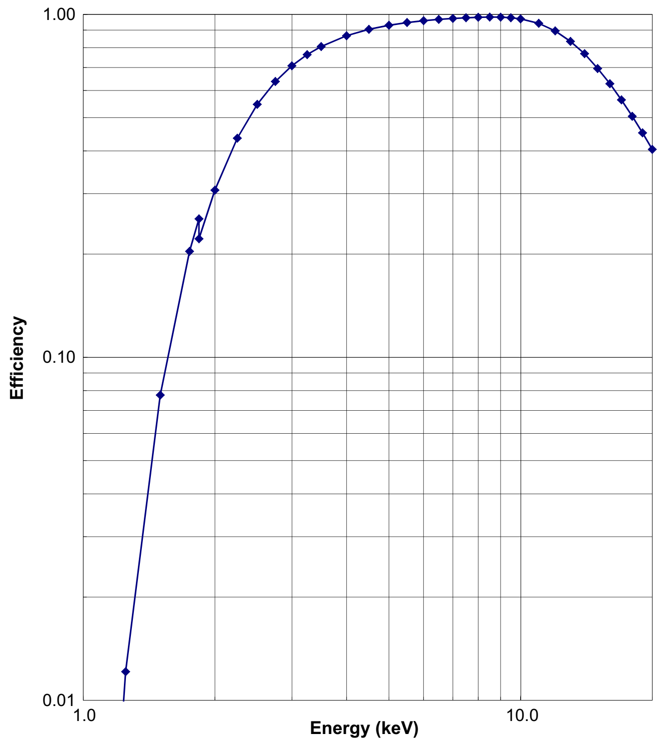

Fig. 14. Modeled efficiency of the MESSENGER Si-PIN solar monitor versus energy. The 76-μm-thick Be window strongly attenuates the lower-energy X-ray flux from the Sun that would otherwise dominate the detector. The Si K-edge is visible at 1.84 keV.

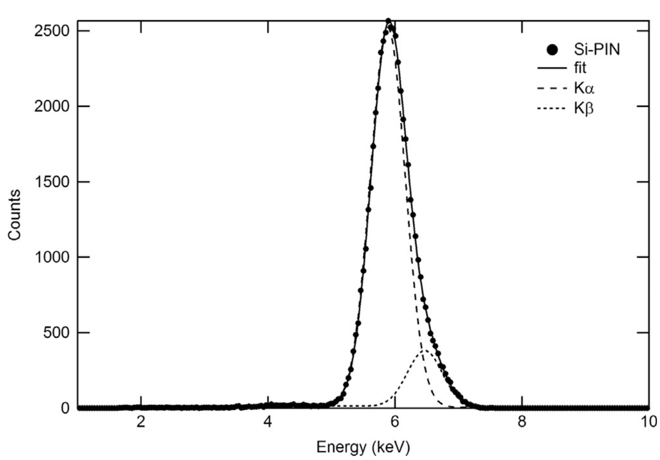

Fig. 15. Response of the MESSENGER Si-PIN solar monitor to an ^{55}Fe source. The fit to the spectrum (solid line) is accomplished by including both the K_α (5.90 keV) and K_β (6.49 keV) Mn lines (dashed lines) plus a polynomial for the background. The fit for the full-energy K_α line gives a FWHM of 635 eV.

the three GPCs. Counting statistics for the August 2007 measurement (indicated by the black vertical bars) in the (a) Mg-filtered and (b) Al-filtered detectors are only fair, but given that limitation the agreement with the February 2005 measurement is good. For

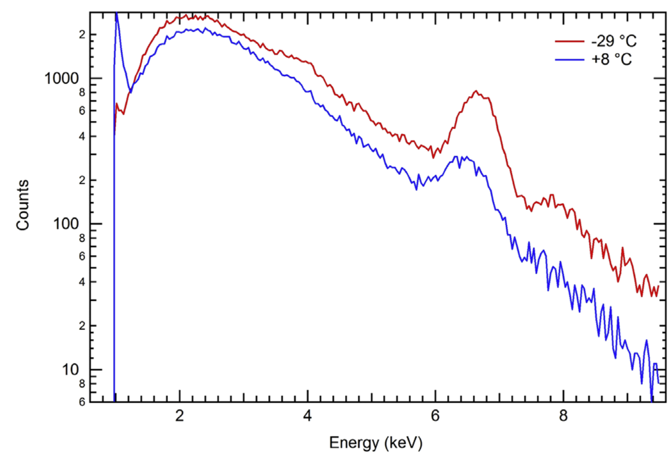

Fig. 16. Solar monitor flare spectra at −29 °C (red) and +8 °C (blue). The peak is at ~6.4 keV. As described in the text, the FWHM of the measurement at +8 °C is ~19% greater than for the measurement at −29 °C.

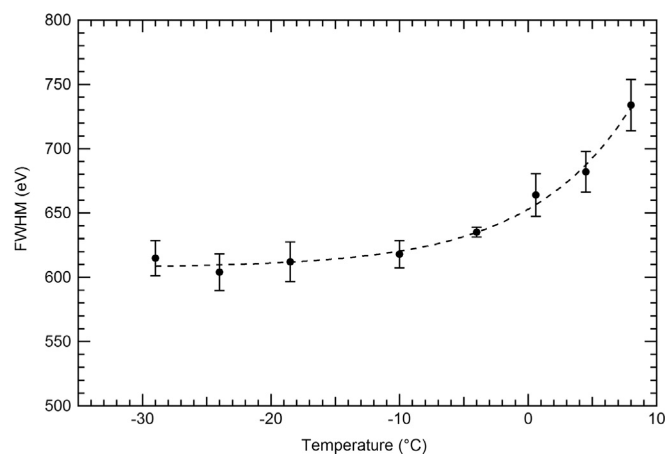

Fig. 17. Solar monitor FWHM versus temperature for seven in-flight solar flare measurements and one laboratory measurement (−4 °C). The data (circles) are well fit by an exponential function (dashed line): FWHM$=607.5+45.46\ e^{0.126\ T}$, where the temperature T is in °C.

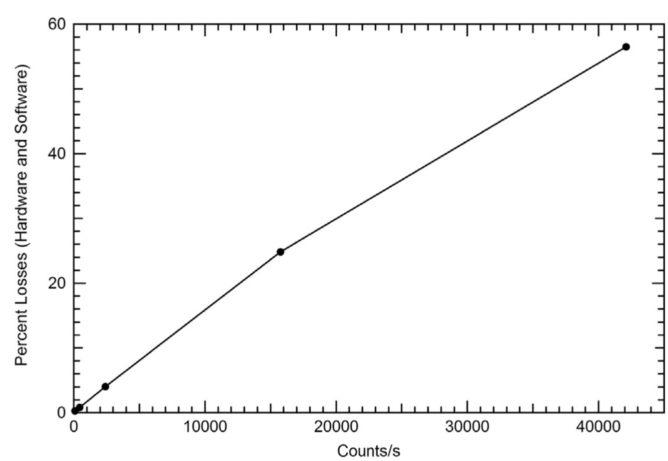

Fig. 18. Percentage of event losses as a function of count rate for the solar monitor.

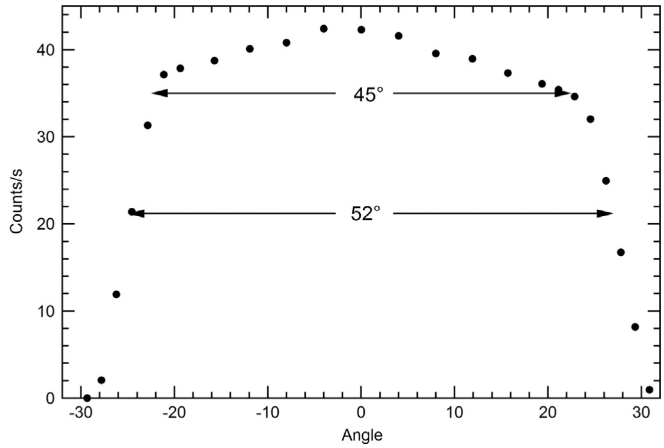

Fig. 19. SAX field of view, expressed as response versus angle from the detector normal.

the (c) unfiltered GPC, for which statistics are substantially superior to those for the other two detectors, agreement between the two measurements is excellent. The combination of rise-time discrimination and anti-coincidence circuitry in the XRS is thus shown to reduce background counts by about an order of magnitude without any appreciable loss of valid counts.

5. Solar monitor calibration measurements

5.1. Efficiency

The MESSENGER solar monitor was a solid-state Si-PIN diode. It was 500 μm thick and had a 76-μm-thick Be window, a 200 nm-thick dead layer, and a ~0.03 mm^2 effective area. The response of the detector was modeled using MCNPX, and the result is shown in Fig. 14. The impact of the Be window on the efficiency at low energies is evident. The efficiency of the solar monitor at 5.9 keV was measured as described above for the gas proportional counters. The result

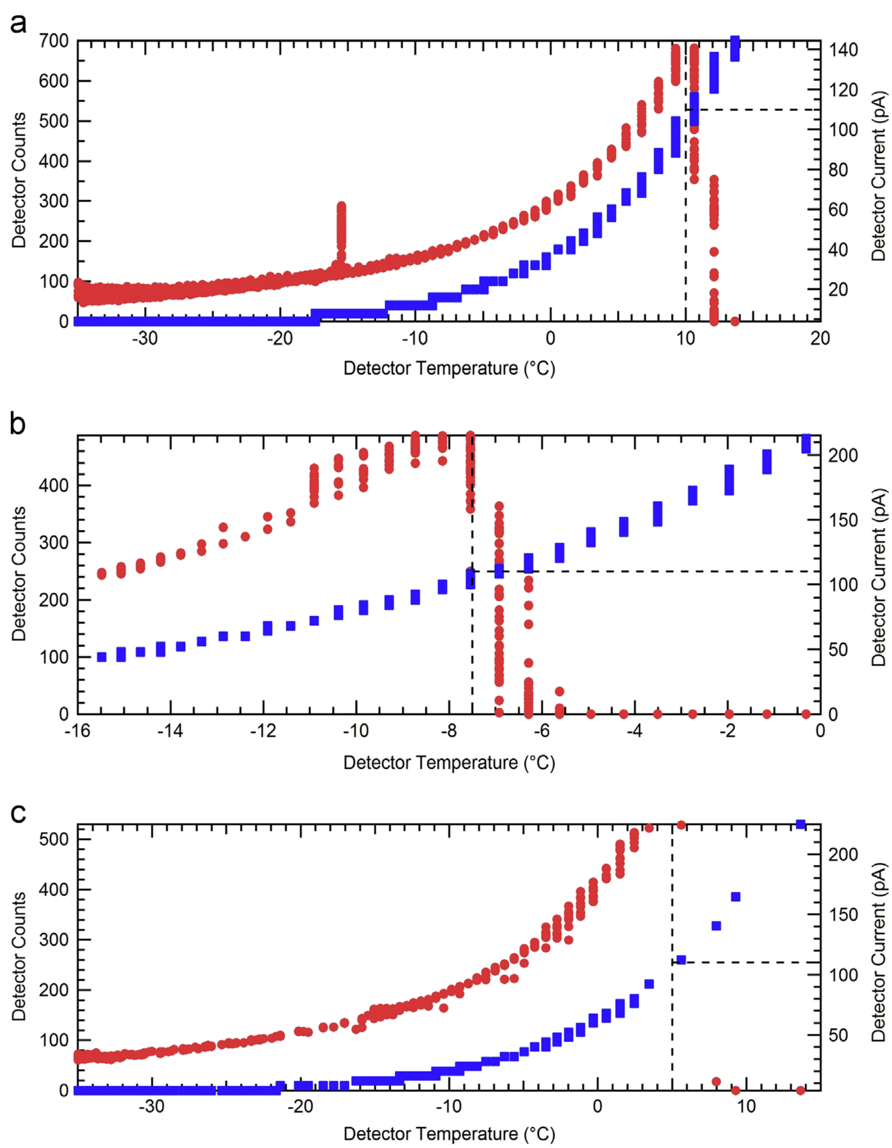

Fig. 20. Solar monitor detector counts (red circles) and detector current (blue squares) versus detector temperature (a) on 14 February 2012, prior to the 5 March 2012 solar particle event; (b) on 13 March 2012, after the solar particle event but before detector annealing; and (c) on 12 May 2012, after annealing. The vertical dashed line shows the temperature at which the leakage current becomes so great that the bias on the FET causes the preamplifier to saturate. The horizontal dashed line indicates the corresponding current at which the FET saturates, about 110 pA.

was 0.982 ± 0.0007, which is in good agreement with the calculated value of 0.96. The error reflects statistical uncertainties only. Systematic errors due to uncertainties in the source-to-detector distance are ~2%.

5.2. Energy resolution

A pulse height spectrum from the Si-PIN detector with an ^{55}Fe source in the field of view is shown in Fig. 15. The K_α and K_β lines merge but are separated by the fit. The FWHM for both the K_α and K_β lines at 5.90 and 6.49 keV, respectively, is 635 eV. This measurement was made at −4 °C. Unlike the proportional counters, the energy resolution of the Si-PIN was determined primarily by the pre-amplifier noise and did not vary significantly over the energy region of interest.

The response of the Si-PIN to two solar flares sufficiently strong to display the 6.4 keV Fe line is shown in Fig. 16. Measurements at two temperatures are compared. The FWHM for the measurement at −29 °C is 615 eV, whereas for the measurement at +8 °C, the FWHM is 734 eV. Fig. 17 plots FWHM for eight solar monitor spectra, seven collected during orbital observations (including the two displayed in Fig. 16), and the laboratory measurement from Fig. 15. At temperatures below −10 °C the FWHM changed little with temperature, but it began to increase at temperatures above −10 °C, and by +8 °C, the highest temperature for which flare data are available, the peak width had increased by ~19%.

5.3. Live time

The solar monitor experienced very high count rates during large solar flares and was designed to be capable of operating at such high rates. Fig. 18 displays the total event loss rate versus count rate for the solar monitor. For a maximum input rate of 42,100 s^{-1}, the loss rate for the solar monitor was 56%. Even for the largest flares observed by the MESSENGER solar monitor, count rates were generally less than 10,000 s^{-1}, at which the loss rate was only ~15%. This reduced lifetime at high rates was not an issue, because event losses did not alter spectral shape. For this reason, it was not necessary to correct for event losses when evaluating solar monitor spectra.

5.4. Field of view

A collimated ^{55}Fe source was also used to measure the FOV of the Si-PIN solar monitor. Fig. 19 shows the measured angular response of the SAX detector from –30° to +30° relative to normal. The measurement displays a 45° full angle response of the detector opening, and a FWHM of ~52°.

5.5. Radiation damage and annealing

On 5 March 2012, a large solar particle event produced severe radiation damage in the XRS solar monitor Si-PIN detector. Prior to this event, the solar monitor provided good solar spectra up to temperatures of ~10 °C. In contrast, following the solar particle event the highest useful operating temperature for the solar monitor was reduced to −7.5 °C. A two-day annealing at 100 °C, beginning on 20 March 2012, improved the situation markedly, so that good solar monitor spectra could be collected up to temperatures of about +5 °C. A second two-day annealing, beginning on 3 April 2012, produced no measureable improvement.

The impact of the solar particle event on solar monitor performance is displayed in Fig. 20, where detector counts (red circles) and detector current (blue squares) are plotted versus detector temperature on three dates: prior to the solar event (a, 14 February 2012), after the solar particle event but before detector annealing (b, 13 March 2012), and after annealing (c, 12 May 2012). Detector counts is an integral over channels 2–15 (~0.9–1.4 keV) in the solar monitor spectra. This spectral region is dominated by electronic noise. The vertical dashed lines show where the leakage current becomes so great that the bias on the FET causes the preamplifier to saturate and effectively turn off the detector, so that detector counts fall to zero. The horizontal dashed line indicates the corresponding current at which the FET saturates, about 110 pA. For the three dates, 14 February, 13 March, and 12 May, this current was reached at 10 °C, −7.5 °C, and 5 °C, respectively.

6. Summary

The MESSENGER XRS has been characterized through a combination of modeling and calibration measurements, made both on the ground and in flight. These efforts have resulted in a detailed understanding of the operational capabilities of the instrument as well as a high level of confidence in the characterization of the XRS response functions. The culmination of these efforts is reflected in the elemental abundance maps produced by the XRS over ~4 years of orbital operations (Nittler et al., 2011; Weider et al., 2012b, 2014, 2015).

Acknowledgments

The authors thank the MESSENGER team for the highly successful operation of the MESSENGER spacecraft throughout cruise, orbit insertion, and Mercury orbital operations. The authors also thank Shoshana Weider for her careful reading of the manuscript and many helpful suggestions. This work was supported in part by the National Aeronautics and Space Administration's Discovery Program through grant number NNX07AR59G to the Catholic University of America. The MESSENGER project is supported under NASA contracts NAS5-97271 to The Johns Hopkins University Applied Physics Laboratory and NASW-00002 to the Carnegie Institution of Washington.

References

Adler, I., Trombka, J., Gerard, J., Lowman, P., Schmadebeck, R., Blodget, H., Eller, E., Yin, L., Lamothe, R., Osswald, G., Gorenstein, P., Bjorkholm, P., Gursky, H., Harris, B., 1972a. Apollo 15 geochemical X-ray fluorescence experiment: preliminary report. Science 175, 436–440.

Adler, I., Trombka, J., Gerard, J., Lowman, P., Schmadebeck, R., Blodget, H., Eller, E., Yin, L., Lamothe, R., Gorenstein, P., Bjorkholm, P., 1972b. Apollo 16 geochemical X-ray fluorescence experiment: preliminary report. Science 177, 256–259.

Adler, I., Trombka, J., Lowman, P., Schmadebeck, R., Blodget, H., Eller, E., Yin, L., Lamothe, R., Osswald, G., Gerard, J., Gorenstein, P., Bjorkholm, P., Gursky, H., Harris, B., Arnold, J., Metzger, A., Reedy, R., 1973. Apollo 15 and 16 results of the integrated geochemical experiment. Moon 7, 487–504.

Dunne, J.A., 1974. Mariner 10 Mercury encounter. Science 185, 141–142.

Foley, C.N., Nittler, L.R., McCoy, T.J., Lim, L.F., Brown, M.R.M., Starr, R.D., Trombka, J.I., 2006. Minor element evidence that Asteroid 433 Eros is a space-weathered ordinary chondrite parent body. Icarus 184, 338–343. http://dx.doi.org/10.1016/j.icarus.2006.05.011.

Grande, M., Kellett, B.J., Howe, C., Perry, C.H., Swinyard, B., Dunkin, S., Huovelin, J., Alha, L., D'Uston, L.C., Maurice, S., Gasnault, O., Couturier-Doux, S., Barabash, S., Joy, K.H., Crawford, I.A., Lawrence, D., Fernandes, V., Casanova, I., Wieczorek, M., Thomas, N., Mall, U., Foing, B., Hughes, D., Alleyne, H., Russell, S., Grady, M., Lundin, R., Baker, D., Murray, C.D., Guest, J., Christou, A., 2007. The D-CIXS X-ray spectrometer on the SMART-1 mission to the Moon–First results. Planet. Space Sci. 55, 494–502. http://dx.doi.org/10.1016/j.pss.2006.08.004.

Knoll, G.F., 1989. Radiation Detection and Measurement. John Wiley & Sons, New York, pp. 160–198.

Leary, J.C., Conde, R.F., Dakermanji, G., Engelbrecht, C.S., Ercol, C.J., Fielhauer, K.B., Grant, D.G., Hartka, T.J., Hill, T.A., Jaskulek, S.E., Mirantes, M.A., Mosher, L.E., Paul, M.V., Persons, D.F., Rodberg, E.H., Srinivasan, D.K., Vaughan, R.M., Wiley, S.

R., 2007. The MESSENGER spacecraft. Space Sci. Rev. 131, 187–217. http://dx.doi.org/10.1007/s11214-007-9269-0.
Lim, L.F., Nittler, L.R., 2009. Elemental composition of 433 Eros: new calibration of the NEAR-Shoemaker XRS data. Icarus 200, 129–146. http://dx.doi.org/10.1016/j.icarus.2008.09.018.
Narendranath, S., Athiray, P.S., Sreekumar, P., Kellett, B.J., Alha, L., Howe, C.J., Joy, K. H., Grande, M., Huovelin, J., Crawford, I.A., Unnikrishnan, U., Lalita, S., Subramaniam, S., Weider, S.Z., Nittler, L.R., Gasnault, O., Rothery, D., Fernandes, V. A., Bhandari, N., Goswami, J.N., Wieczorek, M.A., 2011. Lunar X-ray fluorescence observations by the Chandrayaan-1 X-ray Spectrometer (C1XS): results from the nearside southern highlands. Icarus 214, 53–66.
Nittler, L.R., Starr, R.D., Lim, L., McCoy, T.J., Burbine, T.H., Reedy, R.C., Trombka, J.I., Gorenstein, P., Squyres, S.W., Boynton, W.V., McClanahan, T.P., Bhangoo, J.S., Clark, P.E., Murphy, M.E., Killen, R., 2001. X-ray fluorescence measurements of the surface elemental composition of asteroid 433 Eros. Meteorit. Planet. Sci. 36, 1673–1695.
Nittler, L.R., Starr, R.D., Weider, S.Z., McCoy, T.J., Boynton, W.V., Ebel, D.S., Ernst, C. M., Evans, L.G., Goldsten, J.O., Hamara, D.K., Lawrence, D.J., McNutt Jr., R.L., Schlemm II, C.E., Solomon, S.C., Sprague, A.L., 2011. The major-element composition of Mercury's surface from MESSENGER X-ray spectrometry. Science 333, 1847–1850.
Okada, T., Shirai, K., Yamamoto, Y., Arai, T., Ogawa, K., Hosono, K., Kato, M., 2006. X-ray fluorescence spectrometry of asteroid Itokawa by Hayabusa. Science 312, 1338–1341.
Okada, T., Shirai, K., Yamamoto, Y., Arai, T., Ogawa, K., Shiraishi, H., Iwasaki, M., Kawamura, T., Morito, H., Grande, M., Kato, M., 2010. X-ray fluorescence spectrometry of lunar surface by XRS onboard SELENE (Kaguya). Trans. Japan Soc. Aeronaut. Space Sci. Space Tech. Japan 7, Tk_39–Tk_42.
Pelowitz, D.B. (Ed.), 2005. Monte Carlo N-Particle eXtended (MCNPX) User's Manual Version 2.5.0. Report LA-UR-94-1817, Los Alamos National Laboratory, Los Alamos, New Mexico.
Santo, A.G., Gold, R.E., McNutt Jr., R.L., Solomon, S.C., Ercol, C.J., Farquhar, R.W., Hartka, T.J., Jenkins, J.E., McAdams, J.V., Mosher, L.E., Persons, D.F., Artis, D.A., Bokulic, R.S., Conde, R.F., Dakermanji, G., Goss Jr., M.E., Haley, D.R., Heeres, K.J., Maurer, R.H., Moore, R.C., Rodberg, E.H., Stern, T.G., Wiley, S.R., Williams, B.G., Yen, C.L., Peterson, M.R., 2001. The MESSENGER mission to Mercury: spacecraft and mission design. Planet. Space Sci., 49; pp. 1481–1500.
Schlemm II, C.E., Starr, R.D., Ho, G.C., Bechtold, K.E., Hamilton, S.A., Boldt, J.D., Boynton, W.V., Bradley, W., Fraeman, M.E., Gold, R.E., Goldsten, J.O., Hayes, J.R., Jaskulek, S.E., Rossano, E., Rumpf, R.A., Schaefer, E.D., Strohbehn, K., Shelton, R. G., Thompson, R.E., Trombka, J.I., Williams, B.D., 2007. The X-Ray Spectrometer on the MESSENGER spacecraft. Space Sci. Rev. 131, 393–415.
Schwartz, D.A., 2004. The development and scientific impact of the Chandra X-Ray Observatory. Int. J. Mod. Phys. D13, 1239–1248. http://dx.doi.org/10.1142/S0218271804005377.
Solomon, S.C., McNutt Jr., R.L., Gold, R.E., Acuña, M.H., Baker, D.N., Boynton, W.V., Chapman, C.R., Cheng, A.F., Gloeckler, G., Head III, J.W., Krimigis, S.M., McClintock, W.E., Murchie, S.L., Peale, S.J., Phillips, R.J., Robinson, M.S., Slavin, J.A., Smith, M.T., Strom, R.G., Trombka, J.I., Zuber, M.T., 2001. The MESSENGER mission to Mercury: scientific objectives and implementation. Planet. Space Sci. 49, 1445–1465.
Starr, R.D., Clark, P.E., Evans, L.G., Floyd, S.R., McClanahan, T.P., Trombka, J.I., Goldsten, J.O., Maurer, R.H., McNutt Jr., R.L., Roth, D.R., 1999. Radiation effects in the Si-PIN detector on the Near Earth Asteroid Rendezvous mission. Nucl. Inst. Methods Phys. Res. A 428, 209–215.
Starr, R.D., Clark, P.E., Murphy, M.E., Floyd, S.R., McClanahan, T.P., Nittler, L.R., Trombka, J.I., Evans, L.G., Boynton, W.V., Bailey, S.H., Bhangoo, J., Mikheeva, I., Brückner, J., Squyres, S.W., McCartney, E.M., Goldsten, J.O., McNutt Jr., R.L., 2000. Instrument calibrations and data analysis procedures for the NEAR X-ray spectrometer. Icarus 147, 498–519.
Swinyard, B.M., Joy, K.H., Kellett, B.J., Crawford, I.A., Grande, M., Howe, C.J., Fernandes, V.A., Gasnault, O., Lawrence, D.J., Russell, S.S., Wieczorek, M.A., Foing, B. H., 2009. The SMART-1 team, X-ray fluorescence of the Moon by SMART-1/D-CIXS and the first detection of Ti K_α from the lunar surface. Planet. Space Sci. 57, 744–750. http://dx.doi.org/10.1016/j.pss.2009.01.009.
Trombka, J.I., Squyres, S.W., Brückner, J., Boynton, W.V., Reedy, R.C., McCoy, T.J., Gorenstein, P., Evans, L.G., Arnold, J.R., Starr, R.D., Nittler, L.R., Murphy, M.E., Mikheeva, I., McNutt Jr., R.L., McClanahan, T.P., McCartney, E., Goldsten, J.O., Gold, R.E., Floyd, S.R., Clark, P.E., Burbine, T.H., Bhangoo, J.S., Bailey, S.H., Petaev, M., 2000. The elemental composition of asteroid 433 Eros: results of the NEAR-Shoemaker X-ray spectrometer. Science 289, 2101–2105.
Weider, S.Z., Kellett, B.J., Swinyard, B.M., Crawford, I.A., Joy, K.H., Grande, M., Howe, C.J., Sreekumar, P., Huovelin, J., Narendranath, S., Alha, L., Anand, M., Athiray, P. S., Bhandari, N., Carter, J., Cook, A.C., d'Uston, L.C., Fernandes, V.A., Gasnault, O., Goswami, J.N., Gow, J., Holland, A.D., Koschny, D., Lawrence, D.J., Maddison, B.J., Maurice, S., McKay, D.J., Okada, T., Pieters, C., Rothery, D., Russell, S.S., Shrivastava, A., Smith, D.R., Wieczorek, M., 2012a. The Chandrayaan-1 X-ray spectrometer: first results. Planet. Space Sci. 60, 217–228.
Weider, S.Z., Nittler, L.R., Starr, R.D., McCoy, T.J., Stockstill-Cahill, K.R., Byrne, P.K., Denevi, B.W., Head, J.W., Solomon, S.C., 2012b. Chemical heterogeneity on Mercury's surface revealed by the MESSENGER X-Ray Spectrometer. J. Geophys. Res. 117, E00L05. http://dx.doi.org/10.1029/2012JE004153.
Weider, S.Z., Nittler, L.R., Starr, R.D., McCoy, T.J., Solomon, S.C., 2014. Variations in the abundance of iron on Mercury's surface from MESSENGER X-Ray Spectrometer observations. Icarus 235, 170–186. http://dx.doi.org/10.1016/j.icarus.2014.03.002.
Weider, S.Z., Nittler, L.R., Starr, R.D., Crapster-Pregont, E.J., Peplowski, P.N., Denevi, B.W., Head, J.W., Byrne, P.K., Hauck II, S.A., Ebel, D.S., Solomon, S.C., 2015. Evidence for geochemical terranes on Mercury: global mapping of major elements with MESSENGER's X-Ray Spectrometer. Earth Planet. Sci. Lett. 416, 109–120.
Weisskopf, M.C., Brinkman, B., Canizares, C., Garmire, G., Murray, S., Van Speybroeck, L.P., 2002. An overview of the performance and scientific results from the Chandra X-Ray Observatory. Astron. Soc. Pacific 114, 1–24.
Yin, L.I., Trombka, J.I., Adler, I., Bielefeld, M., 1993. X-ray remote sensing techniques for geochemical analysis of planetary surfaces. In: Pieters, C.M., Englert, P.A.M. (Eds.), Remote Geochemical Analysis: Elemental and Mineralogical Composition. Cambridge Univ. Press, Cambridge, U.K, pp. 199–212.